Flow-induced vibrations of low aspect ratio rectangular membrane wings

P. Rojratsirikul[†], M.S. Genc[†§], Z. Wang[†] and I. Gursul[†*]

[†]Department of Mechanical Engineering, University of Bath, Bath, BA2 7AY, United Kingdom

[§]Department of Energy Systems Engineering, Erciyes University, Kayseri, Turkey

ABSTRACT

An experimental study of a low aspect ratio rectangular membrane wing in a wind tunnel was conducted for a Reynolds number range of 2.4×10^4 to 4.8×10^4. Time-accurate measurements of membrane deformation were combined with the flow field measurements. Analysis of the fluctuating deformation reveals chordwise and spanwise modes, which are due to the shedding of leading-edge vortices as well as tip vortices. At higher angles of attack, the second mode in the chordwise direction becomes dominant as the vortex shedding takes place. The dominant frequencies of the membrane vibrations are similar to those of two-dimensional membrane airfoils. Measured frequency of vortex shedding from the low aspect ratio rigid wing suggests that membrane vibrations occur at the natural frequencies close to the harmonics of the wake instabilities. Vortex shedding frequency from rigid wings shows remarkably small effect of aspect ratio even when it is as low as unity.

[*] Corresponding author.
Email address: i.a.gursul@bath.ac.uk

Nomenclature

b = wing span

c = chord length

C_n = normal force coefficient

E = Young's modulus

f = frequency

F_n = normal force

q = dynamic pressure ($\frac{1}{2}\rho U_\infty^2$)

Re = Reynolds number ($U_\infty c/\nu$)

St = Strouhal number (fc/U_∞)

S = wing area

t = membrane thickness

U_∞ = freestream velocity

z = membrane displacement in a direction normal to the chordline

z_{max} = maximum membrane displacement

z_{sd} = standard deviation of membrane displacement

$z_{sd,max}$ = maximum standard deviation of membrane displacement

α = angle of attack

μ = viscosity

ν = kinematic viscosity (μ/ρ)

Π_1 = aeroelastic parameter $(Et/q_\infty c)^{1/3}$

ρ = density of air

ρ_m = density of membrane

1. Introduction

There is a growing interest in the use of membrane wings, particularly for Micro Air Vehicles (MAVs) because of their light weight as well as passive shape adaptation (Shyy et al., 1999; Lian et al., 2003). MAVs typically operate at Reynolds numbers below 10^5, where unfavorable aerodynamic characteristics such as low lift, flow separation, leading-edge separation bubbles and unsteadiness present major problems. Studies of fixed-wing membrane MAVs have been carried out recently. It was found that membrane wings can significantly improve longitudinal static stability (Albertani et al., 2007; Stanford et al., 2007), provide more favorable lift-to-drag ratio (Shyy et al., 1999; Lian et al., 2003; Stanford et al., 2008), and delay stall (Lian et al., 2003). Even membrane skin with low degree of compliance can have substantial effects on the aerodynamic performance.

Early studies concentrated on two-dimensional membrane airfoils. Several studies employed the potential flow theory to solve an equation for two-dimensional sails in equilibrium and steady conditions (Newman and Low, 1984; Greenhalgh et al., 1984; Newman, 1987; and Jackson and Christie, 1987). Later work by Smith and Shyy (1995, 1996) studied the same problem for steady laminar flow and turbulent flow. It was found that the potential flow theory can only be sufficient for inextensible membranes with small camber and incidence. For larger cambers and incidences, viscous effects and flow separation need to be considered.

Unsteady fluid-structure interactions and flow-induced vibrations of the membrane airfoils were not considered in these early studies. Recent work undertaken at the University of Bath using a nominally two-dimensional membrane airfoil demonstrated that flexibility creates strong coupling of membrane oscillation and unsteady separated flow (Rojratsirikul et al., 2009). In a subsequent study, the effect of pre-strain and excess length on the same membrane airfoil

configuration was explored experimentally (Rojratsirikul et al., 2010a). The close coupling between vortex shedding and membrane response was also demonstrated in simulations by Gordnier (2009). Figure 1 taken from previous work (Rojratsirikul et al., 2010a) shows the power spectra of the membrane vibrations as a function of angle of attack at different freestream velocities. This plot reveals the band of dominant frequencies at which vibrations occur for each incidence. It is seen that the vibration occurs at certain modes corresponding to the natural frequency of the membrane and its harmonics, and generally at the second mode at post-stall incidences. The cross symbols superimposed on the same figure are the shedding frequencies in the wake of an equivalent rigid cambered airfoil, which are measured by hot-wire anemometry at the corresponding freestream velocity and angle of attack. This figure suggests that the membrane vibrations might be coupled with the first harmonic of the natural vortex shedding frequency at high incidences. This is perhaps not surprising as several flow control studies revealed the vortex lock-in phenomenon for airfoils in post-stall regime (Wu et al., 1999; Miranda et al., 2005) when the excitation frequency is equal to the natural frequency of vortex shedding in the wake and its harmonics. The dashed line in Figure 1 is a curve fit to the data, which yields a modified Strouhal number based on the projection distance:

$$fc \sin\alpha / U_\infty = 0.17. \qquad (1)$$

This knowledge can be used in designing membrane wings to exploit the vortex lock-in phenomenon, since it was shown that the membrane oscillations excite the separated shear layer and delay the stall compared to a rigid cambered airfoil. Hence this is a potential passive flow control method using flexibility.

Relevant to more practical MAV applications, recent studies focused on the three-dimensional membrane wings. Song et al. (2008) conducted experiments on low aspect ratio (AR

= 0.9, 1.4, and 1.8) rectangular membrane wings. They observed vibration modes, which appeared predominantly in the chordwise direction with small variations in the spanwise direction. The membrane natural frequencies were predicted well by using the linear elastic theory and estimated tension from the mean deformation (although Song et al. adjusted the value of the pre-strain significantly). Our predictions based on the linear theory (Rojratsirikul et al., 2009, 2010a) differed significantly (as much as by a factor of 2 of the measured frequencies), which we believe highlights the nonlinear effects for the fluid-structure interaction. Nevertheless, for the low aspect ratio rectangular membrane wings, the main features of the vibrations appear to be similar to those of two-dimensional airfoils. These are: i) predominantly chordwise vibration modes, ii) specific number (order) of the modes, iii) increasing mode numbers with increasing freestream velocity, and iv) the observations of the second mode at higher incidences. In fact, even the Strouhal number corresponding to the dominant frequency is similar (as an example, $fc/U_\infty \approx 0.8$ for $\alpha = 24°$ in Song et al., which compares well with the data in Figure 1).

As discussed earlier, we suggest that there is a coupling between the membrane vibrations and wake instabilities, and that membrane vibrations occur at the natural frequencies close to the harmonics of wake instabilities. One wonders if this is also true for low aspect ratio wings. It is known that vortex shedding from bluff bodies becomes weaker as the aspect ratio is reduced, but does not disappear (Bearman, 1984). Fail et al. (1959) tested low aspect ratio flat plates normal to the freestream and detected vortex shedding in the wake even for aspect ratio of unity. Although there are some studies on the effect of aspect ratio for bluff bodies (Vickery, 1968; Wootton, 1986), we have found no systematic/detailed studies for low aspect ratio wings. The only exception is the numerical study of Taira and Colonius (2009), who reported evidence of periodic vortex shedding behind low aspect ratio (AR = 1 to 4) rectangular wings at extremely

low Reynolds numbers of Re = 300 and 500. In contrast, we are interested in larger Reynolds numbers in the range of Re = 10 000 to 100 000, which are more realistic for fixed wing micro air vehicles. In the present study, we have measured the vortex shedding frequency in the wake of low aspect ratio (AR= 1 and 2) flat plate wings at low Reynolds numbers (less than 10^5), and compared with available data for higher aspect ratio wings and nominally two-dimensional airfoils. We also measured the unsteady deformation of a rectangular membrane wing with AR=2 and compared the vibration frequencies with those from the wake measurements of the rigid wing. For completeness we also provided the time-averaged flow and turbulence intensity obtained from the time-accurate PIV measurements.

2. Experimental apparatus and methods

2.1. Models

The experiments were carried out in a low-speed, closed-loop open-jet wind tunnel with a circular working section of 760 mm in diameter, located at the Department of Mechanical Engineering, University of Bath. The wing model tested was a rectangular wing with aspect ratio of AR = 2, and a chord length of c = 68.8 mm (main dimensions are shown in Figure 2). The wing was composed of a rigid frame and an attached membrane. The rigid frame was made from stainless steel, manufactured to have an airfoil-shape cross-section with the sharp edge pointing inwards as shown in Figure 2. The membrane was made from a black latex rubber sheet with a thickness of t = 0.2 mm, Young's modulus of E = 2.2 MPa, and density of ρ_m = 1 gr/cm^3. The wing with its support was attached to a rod, which was attached to two circular plates and end plates as shown in Figure 3. The whole set-up was placed in the open section of the wind tunnel. The circular plates were used to adjust the angle of attack and the distance between the end plates was 450 mm.

The experiments were conducted over angles of attack ranging from $\alpha = 0°$ to post-stall incidences, and freestream velocities of U_∞ = 5, 7.5, and 10 m/s, which correspond to Reynolds numbers based on the chord length of Re = 24 300, 36 500, and 48 700, respectively. The aeroelastic parameter, $\Pi_1 = (Et/qc)^{1/3}$, used by Smith and Shyy (1995, 1996) has a value of Π_1 = 7.51, 5.73, and 4.73 respectively. A rigid wing was also manufactured in an effort to make a comparison with membrane wings. The rigid flat-plate wing was made of 1 mm thick stainless steel.

2.2. Deformation measurements

Digital Image Correlation (DIC) system was used to measure the membrane displacements. DIC is a non-intrusive full-field measurement technique (Peters and Ranson, 1982; Chu et al., 1985), which employs a correlation method to measure deformation on the surface of an object. The underlying principle is to track the deformation of grey value pattern applied to the surface by capturing consecutive images and then calculate the displacement field of the specimen. Two pre-calibrated CCD cameras acquire the speckling patterns when no load is applied to the specimen, referred to as a reference image. The cameras then acquire the patterns after loading, and the analysis finds a region that maximizes a normalized cross-correlation function corresponding to a small subset or facet of the reference images. The coordinates of the reference frame are then transformed to coordinates within the deformed image.

The present experiment employed 3-D digital image correlation which allows the measurement of all three surface displacement fields simultaneously. Two calibrated and synchronized cameras (FASTCAM SA1.1, Photron 192.168.0.11 lens: Nikon AF NIKKOR24 24-85mm 1:2.8-4 D) were mounted above and behind the set-up, looking from a different

viewing angle (as shown in Figure 3). Two floodlights were used to illuminate the model. The cameras captured images at a rate of 1500 frames per second, corresponding to exposure time of 0.667 ms, producing sequences of 1500 instantaneous deformation fields over 1 second.

The commercial software package VIC3D2007 was used for the analysis of the digital images obtained. The subset size (or correlation window size) varied from 17-21 pixels, and the grid step from 4-6 pixels, resulting in an effective grid size around 1% of the chord length in these experiments. The uncertainty of the deformation measurements in the out-of-plane direction is estimated to be 0.04% of the chord length. Typical data consist of the geometry of the surface in discrete coordinates and the corresponding displacements. Post-processing within the software involved transformation of coordinates to define the chordwise direction and calculation of the out-of-plane displacement. Final post-processing was complemented in MATLAB to calculate mean displacement (z), extract the maximum value (z_{max}), calculate standard deviation (z_{sd}) and find the maximum value ($z_{sd,max}$).

2.3. Force measurements

A load cell was used to make direct force measurements in the normal direction to the chordline. The calibration was performed by loading the load cell with known weights. Calibration was repeated before each set of experiments to ensure consistency. Sets of data chosen at random were repeated. The force data was collected at a sampling frequency of 3000 Hz over 20 seconds. The normal force coefficient is given by

$$C_n = \frac{F_n}{\frac{1}{2}\rho U_\infty^2 S}. \qquad (2)$$

The measurement uncertainty for the normal force coefficient is estimated to be 2%. The estimate was based on the standard uncertainty calculations such as Kline-McClintock method (Kline and McClintock, 1953).

2.4. Velocity measurements

Quantitative flow measurements were undertaken using Digital Particle Image Velocimetry (DPIV). A pair of pulsed mini Nd: YAG lasers with a maximum energy output of 120 mJ per pulse was used to illuminate the desired plane. The laser sheet was placed parallel to the freestream flow in the wing symmetry plane as shown in Figure 4. A combination of cylindrical and spherical lenses was used to adjust both the thickness and the width of the laser sheet. Images were captured using an 8-bit TSI PowerView 4M CCD camera, placed perpendicular to the laser sheet, with a resolution of 2048×2048 pixels and a maximum capture rate of 7.5 frames per second, producing 3.75 frames per second in the cross-correlation mode. Sequences of 200 velocity fields were produced for each measurement. The commercial software TSI Insight v6.0 and a fast Fourier transform (FFT) cross-correlation algorithm were used to analyze the images, with an interrogation window size of 32 by 32 pixels, resulting in the effective grid size of approximately 2% of the chord length. The uncertainty of the velocity measurements is estimated to be 2% of the freestream velocity.

Hot-wire measurements were conducted for spectral analysis of the velocity fluctuations in the wake of the rigid wing. These measurements were taken with a single hot-wire probe located at one chord-length and two chord-lengths distances from the trailing-edge. The location of the probe was traversed across the wake, and the velocity spectra were calculated for each location. These measurements were also performed for a lower aspect ratio wing with AR = 1 in order to investigate the effects of the aspect ratio.

3. Results

3.1. Time-Averaged Deformation

Figure 5 shows examples of the time-averaged membrane displacement in the direction normal to the chord-line, for U_∞ = 5 m/s. Even though there are in-plane motions (in the x and y directions) due to the nature of membrane skin, the deformation in the out-of-plane direction is considerably more dominant. As expected, the magnitude of the time-averaged displacement increases with increasing angles of attack. The displacement contours are approximately symmetrical with respect to a mid-span plane, which suggest that time-averaged flow and tip vortices are fairly symmetrical. The peak locations are slightly towards the leading-edge. This is consistent with the previous study of the two-dimensional membrane airfoil (Rojratsirikul et al., 2009), for which the maximum cambers occur slightly forward of the mid-chord. The variation of the maximum magnitudes of z-displacement as a function of angle of attack is shown in Figure 6 for different freestream velocities. For the lowest freestream velocity U_∞ = 5 m/s, the maximum displacement increases gradually up to about $\alpha = 20^o$, then stays roughly constant. The membrane generates a larger magnitude of the maximum camber as the freestream velocity is increased. Notably, there is also camber at zero angle of attack particularly at U_∞ = 10 m/s.

3.2. Velocity field

Figure 7 shows the comparison of the magnitude of the time-averaged velocity field superimposed on the streamline pattern for the rectangular wings at selected angles of attack. The data were taken for the rigid wing at U_∞ = 5 m/s, and the membrane wing at U_∞ = 5 m/s and 10 m/s. Starting with small incidence $\alpha = 5^o$, the flow appears to remain attached for all wings, although there is possibly a small separation region for the rigid wing. At higher angle of attack $\alpha = 10^o$, the flow on the rigid wing becomes totally separated. For $\alpha = 16^o$, the shear layer moves

away from the surface for the rigid wing, while the flow on the membrane wing is separated but the shear layer remains close to the surface. It is also seen that at this angle of attack, with increasing freestream velocity to U_∞ = 10 m/s, the shear layer for the membrane wing is getting closer to the wing surface while the camber of the wing increases. The effect of increasing freestream velocity is consistent with the previous work for two-dimensional membrane airfoils (Rojratsirikul et al., 2009, 2010a). The separated shear layer moves further away from the surface with increasing angle of attack to $\alpha = 23^o$ for all wings. Again, the separation region is largest for the rigid wing, and smallest for the membrane wing with U_∞ = 10 m/s. For the latter, the closed streamline pattern (recirculation region) is seen over the wing surface, while it is located further downstream for the lower freestream velocity, and even further away from the trailing edge for the rigid wing.

Figure 8 shows the turbulence intensity corresponding to the velocity fields illustrated in Figure 7. For all wings, with increasing angle of attack the shear layer velocity fluctuations move away from the surface and also become stronger. Even though the time-averaged velocity for the membrane wing at $\alpha = 10^o$ shows that the flow is mostly attached, significant velocity fluctuations develop near the surface at U_∞ = 5 m/s as shown in Figure 8. With increasing camber at a given angle of attack, the region of velocity fluctuations moves closer to the wing surface. For the largest angle of attack $\alpha = 23^o$ and largest freestream velocity U_∞ = 10 m/s, the velocity fluctuations are strong and located in a region just above the wing. The location of the high intensity velocity fluctuations with respect to the membrane surface affects the amplitude and mode of the membrane vibrations as shown in our previous work. In the present paper this aspect will be discussed later on.

3.3. Normal force coefficient

For completeness, the variation of the time-averaged normal force coefficient is shown as a function of angle of attack in Figure 9 for the membrane and rigid rectangular wings at different freestream velocities. The slope of the normal force coefficient is nearly linear until the stall. The flexible membrane wings have higher slopes than the rigid wing, and the stall angles are only slightly affected. With increasing free stream velocity, the stall angle becomes smaller. These favorable larger slopes are not unexpected as the induced wing camber increases with increasing angle of attack. However, the corresponding increase in the camber alone does not explain the significant increase in the force slope. It was shown by Rojratsirikul et al. (2010b) that the vortex lift due to the tip vortices contributes significantly to the total lift. With increasing membrane deformation, stronger tip vortices develop, which increase the lift slope further. The membrane wings tested in the present experiments exhibit the largest C_n slope for the largest camber. At the highest freestream velocity, U_∞ = 10 m/s, the membrane wing reaches the highest maximum normal force coefficient $C_{n,max}$ of approximately 1.26, which is about 1.5 times that of the rigid wing.

As noted earlier, the rigid wing was a flat-plate, and did not have the mount in comparison with the membrane wings. The effect of the mount, which theoretically may induce an effective camber, is negligibly small. This can be seen from the force measurements for the lowest free stream velocity (U_∞ = 5 m/s). At very small incidences, the membrane deformation is very small and the shape is close to a flat plate. The force data agree very well with that of a flat plate as seen in Figure 9. This justifies the use of a flat plate for the rigid case.

3.4. *Unsteady deformation*

Magnitudes of standard deviation (z_{sd}) of membrane displacement in the z-direction normalized by the chord length are plotted in Figure 10 for different freestream velocities and angles of attack. The membrane vibrations are due to the unsteady flow over the wing. For low aspect ratio (LAR) wings, the unsteadiness is associated with the leading-edge separation as well as tip vortices. Combination of tip vortices and vortex shedding results in rather complicated unsteady deformation for this LAR membrane wing. The vibrational modes are symmetric with respect to the wing symmetry plane in most cases, although asymmetries are observed at some moderate to high angles of attack.

Figure 10(a) illustrates the z_{sd}-contours for U_∞ = 5 m/s, at a low incidence (α = 10^o), intermediate incidence (α = 17^o) and relatively high incidence (α = 23^o). At α = 10^o, dominant vibrational modes could be identified as a spanwise mode of three and a chordwise mode of three. The spanwise and chordwise modes are obtained by counting the peaks of standard deviation of membrane displacement in spanwise and chordwise directions, respectively. The two peaks near the wing tips suggest the membrane oscillations are induced by the tip vortices, whereas the other peaks suggest the vibrations are induced by vortex shedding from the leading-edge. At the higher angle of attack (α = 17^o) the vibrational modes in the spanwise direction are no longer visible, and only the chordwise mode of two is observed. Cross-flow measurements presented by Rojratsirikul et al. (2010b), show that, with increasing angle of attack, tip vortices move away from the membrane surface. This may explain decreasing influence of the tip vortices on the vibration modes at higher angles of attack. In the previous study of the two-dimensional membrane airfoil, there was evidence of coupling of membrane oscillations with the vortex shedding in the wake at high incidences and the dominant mode was also the second

mode (Rojrasirikul et al., 2009). We propose that the rectangular membrane wing at $\alpha = 17^o$ might respond to the vortex shedding in the wake as well and this will be discussed later on with the help of the spectral analysis of the membrane vibrations. Similarly, for $\alpha = 23^o$, the second mode is also noticed with smaller magnitude. For $U_\infty = 7.5$ m/s, at a small incidence ($\alpha = 4^o$), small amplitude oscillation is observed in the first mode (see Figure 10(b)). For the higher angle of attack, $\alpha = 12^o$, there are mixed vibrational modes in the chordwise and spanwise directions. This oscillating pattern is similar to the pattern for $U_\infty = 5$ m/s, $\alpha = 10^o$ as discussed earlier. Again, the second mode in the chordwise direction is noted at the higher angle of attack, $\alpha = 15^o$. For $U_\infty = 10$ m/s, the second mode is observed early at $\alpha = 9^o$ (see Figure 10(c)). For the higher incidence, $\alpha = 14^o$, the higher vibrational modes are observed over the wing surface. This complicated pattern might be the result of the membrane responding to a mixture of tip vortices and vortex shedding from the leading-edge.

In general, there is a relationship between the shear layer velocity fluctuations and membrane vibrations. This can be seen from the comparison of membrane vibrations in Figure 10 and velocity fluctuations in Figure 8. The membrane vibrations are the largest for the largest freestream velocity, when the shear layer is the closest to the wing surface. Also, the largest membrane vibrations are observed for intermediate incidences, because the shear layer moves further away from the wing surface at high incidences.

Figure 11 shows the frequency spectra computed from the z-displacement of the membrane sampled at the point of maximum standard deviation. For small incidences, the dominant normalized frequencies (Strouhal numbers $\mathrm{St} = fc/U_\infty$) are rather difficult to identify. However, starting around $\alpha = 7^o$ to 9^o, the dominant normalized frequencies fall in a well-defined band, and on the order of unity for all freestream velocities. Within certain ranges of angles of

attack (such as α = 11° to 14° at U_∞ = 5 m/s in Figure 11(a)), there seems to be higher modes. Of course, the change in the dominant frequencies is related to the change in the mode shapes. For example, the third mode of vibration for U_∞ = 5 m/s and α = 10° shown in Figure 10(a) corresponds to the dominant frequency of approximately St = 1.1 in Figure 11(a). On the other hand, the second modes for U_∞ = 5 m/s at α = 17° and α = 23° match with the dominant frequencies of St = 0.85 and 0.83, respectively. The relation between the mode shape and its corresponding dominant frequency is also visible for the higher freestream velocities (U_∞ = 7.5 m/s and 10 m/s). In addition, the standard deviation contours (shown in Figure 10) suggest that the membrane tends to exhibit stronger vibrations at higher freestream velocities. This is confirmed by the frequency spectrum plot shown in Figure 11, in which we observe higher spectral density (darker bands) as the freestream velocity increases. The stronger vibrations with increasing free stream velocity are not only due to the increased dynamic pressure. As the freestream velocity increases, shear layer also gets closer to the membrane surface. The Strouhal number decreases slightly with increasing U_∞, particularly for incidences equal and larger than α = 15°. At high incidences, where the second mode is always observed, the Strouhal numbers are in a similar range with those of the two-dimensional membrane airfoils (Rojratsirikul et al., 2010a) as shown in Figure 1. For two-dimensional membrane airfoils, the oscillation in this range suggests the coupling with the vortex shedding in the wake.

3.5. Frequency of vortex shedding from rigid wing

We found the vortex shedding frequency from the dominant frequency in the spectra of the velocity fluctuations in the wake of the rigid flat-plate wings (AR = 1 and 2). The location of the hot-wire probe was varied in two downstream stations (one chord-length and two chord-lengths from the trailing-edge). In doing so the probe was kept in the quarter-span plane in the

spanwise direction, rather than the mid-span plane (in order to avoid the proximity to the wing support). A typical example is shown in Figure 12 for $\alpha = 15°$ and Re = 48,700. The dominant frequency obtained from such measurements and spectra was averaged for at least 10 measurement locations.

The variation of the frequency of vortex shedding from the rigid wing (AR = 2) is added into Figure 11. At high incidences, membrane vibrations occur in the mode/frequency that is closest to the first harmonic of the wake instability. The present results confirm the possibility of coupling of membrane oscillations for the rectangular wing with the wake instabilities. The variation of the Strouhal number for the two wings (AR = 1 and 2) are shown as a function of angle of attack in Figure 13. Here we added available data from other investigations for different aspect ratios. Table 1 lists the aspect ratio, airfoil cross-section, maximum thickness-to-chord ratio, Reynolds number, and measurement station for these references. Also, the best curve-fit to the data for the two-dimensional thin airfoils (Equation (1)) is shown in Figure 13 with the dashed line. The data for the finite wings are remarkably close to this curve-fit and the effect of the aspect ratio appears to be negligible.

As the dashed line and the corresponding modified Strouhal number of 0.17 (in Equation (1)) come from the measurements for the rigid, thin, cambered airfoils (Rojratsirikul et al., 2009), it would be interesting to compare with the uncambered (symmetric) airfoils. Table 1 lists the previous work on flat-plate airfoils. Figure 14 compares the Strouhal number as a function of angle of attack from previous work. Again, it is seen that the modified Strouhal number is approximately 0.17 for two-dimensional flat-plate airfoils, and the effect of camber and thickness is small.

Finally we return to the data for the finite wings and present the variation of the modified Strouhal number as a function of angle of attack in Figure 15. The data fall in between 0.15 and 0.20 over a large range of incidences, with an average value of 0.17 approximately. Taira and Colonius (2009) reported the modified Strouhal number to be 0.12 in their numerical simulations for Re = 300 and 500. They interpreted this deviation from the two-dimensional case as the effects of three-dimensional wake dynamics and tip vortices. However, our data suggest that the Strouhal number of shedding frequency increases with Reynolds number. At reasonably high Reynolds numbers (but still relevant to fixed wing micro air vehicles), we find that the shedding frequency is not affected by the aspect ratio. In Figure 15, although the deviations from the average value of 0.17 are generally small, there is a consistent trend for all wings. A local minimum around $\alpha \approx 14°$ and a local maximum around $\alpha \approx 20°$ are visible. Further research into these aspects will be required in future work.

4. Conclusions

Flow-induced membrane vibrations were studied experimentally for a low aspect ratio rectangular wing at low Reynolds numbers. Analysis of the fluctuating deformation reveals different vibration mode shapes as a function of the freestream velocity and angle of attack. These mode shapes are closely related to the magnitude and location of the shear layer fluctuations over the membrane surface. The standard deviation of the fluctuating deformation indicates the existence of both chordwise and spanwise vibrational modes for the rectangular wing. In general, the combination of tip vortices and vortex shedding results in a mixture of chordwise and spanwise vibrational modes. At higher angles of attack, the membrane oscillations are observed in a chordwise mode. The second mode always appears at high incidences, for all freestream velocities, which is similar to the observations for the two-dimensional membrane

airfoils. It is suggested that the membrane responds to the vortex shedding in the wake in the post-stall region. The dominant frequencies of the membrane vibrations exhibit strong similarities with those of two-dimensional membrane airfoils.

Measured frequency of vortex shedding from the rigid wing supports the hypothesis of a coupling of membrane vibrations with the wake instabilities. The rigid wing data show that vortex shedding frequency is remarkably close to that of two-dimensional airfoils. Analysis of available data reveals negligible effect of camber and thickness of the airfoil at low Reynolds numbers relevant to the fixed-wing MAVs. Negligible effect of aspect ratio (down to AR = 1) is noted for the rectangular wings in the Reynolds number range of 10^4 to 10^5, although there is evidence that at extremely low Reynolds numbers (few hundreds) this may not be valid.

Acknowledgments

The authors would like to acknowledge funding from the US Air Force Office of Scientific Research (AFOSR) under Grant no. FA8655-07-1-3044 and FA8655-09-1-3007, the Research Councils UK Academic Fellowship in Unmanned Air Vehicles (ZW), the Scientific and Technological Research Council of Turkey (TUBITAK) Post-doctoral Fellowship (MSG), and the Royal Thai Government Scholarship (PR). The authors would like to thank the EPSRC Engineering Instrument Pool.

References

Abernathy, F.H., 1962. Flow over an inclined plate. ASME Journal of Basic Engineering 84, 380 - 388.

Albertani, R., Stanford, B., Hubner J.P., Ifju, P.G., 2007. Aerodynamic coefficients and deformation measurements on flexible micro air vehicle wings. Experimental Mechanics

47(5), 625-635.

Bearman, P.W., 1984. Vortex shedding from oscillating bluff-bodies. Annual Review of Fluid Mechanics 16, 195-222.

Calderon, D.E., Wang, Z., Gursul, I., 2010. Lift enhancement of a rectangular wing undergoing a small amplitude plunging motion. AIAA-2010-386, 48th AIAA Aerospace Sciences Meeting, 4-7 January, Orlando, FL, USA.

Chen, J.M., Fang, Y.C., 1996. Strouhal numbers of inclined flat plates. Journal of Wind Engineering and Industrial Aerodynamics 61, 99-112.

Chu, T. C., Ranson, W. F., Sutton, M. A., Peters, W. H., 1985. Applications of digital-image-correlation techniques to experimental mechanics. Experimental Mechanics 25(3), 232-244.

Fage, A., Johansen, F.C., 1927. On the flow of air behind an inclined flat plate of infinite span. Proceedings of the Royal Society of London Series A 116, 170-197.

Fail, R., Lawford, J.A., Eyre, R.C.W., 1959. Low speed experiments on the wake characteristics of flat plates normal to an air stream. British ARC R&M 3120.

Gordnier, R.E., 2009. High fidelity computational simulation of a membrane wing airfoil. Journal of Fluids and Structures 25, 897-917.

Greenhalgh, S., Curtiss, H.C., Smith, B., 1984. Aerodynamic properties of a two-dimensional inextensible flexible airfoil. AIAA Journal 22(7), 865-870.

Huang, R.F., Lin, C.L., 1995. Vortex shedding and shear-layer instability of wing at low-Reynolds numbers. AIAA Journal 33(8), 1398-1403.

Jackson, P.S., Christie, G.W., 1987. Numerical analysis of three-dimensional elastic membrane wings. AIAA Journal 25(5), 676-682.

Kline, S.J., McClintock, F.A., 1953. Describing uncertainties in single sample experiments. Mechanical Engineering 75, 3-8.

Lian, Y. S., Shyy, W., Viieru, D., Zhang, B., 2003. Membrane wing aerodynamics for micro air vehicles. Progress in Aerospace Sciences 39(6-7), 425-465.

Miranda, S., Vlachos, P.P., Telionis, D.P., Zeiger, M.D., 2005. Flow control of a sharp-edged airfoil. AIAA Journal 43(4), 716-726.

Newman, B.G., 1987. Aerodynamic theory for membranes and sails. Progress in Aerospace Sciences 24, 1-27.

Newman, B.G., Low, H.T., 1984. Two-dimensional impervious sails: experimental results compared with theory. Journal of Fluid Mechanics 144, 445-462.

Peters, W. H., Ranson, W. F., 1982. Digital imaging techniques in experimental stress analysis. Optical Engineering 21, 427-431.

Rojratsirikul, P., Wang, Z., Gursul, I., 2009. Unsteady fluid–structure interactions of membrane airfoils at low Reynolds numbers. Experiments in Fluids 46(5), 859-872.

Rojratsirikul, P., Wang, Z., Gursul, I., 2010a. Effects of pre-strain and excess length on unsteady fluid-structure interactions of membrane airfoils. Journal of Fluids and Structures 26, 359-376.

Rojratsirikul, P., Wang, Z., Gursul, I., 2010b. Unsteady aerodynamics of low aspect ratio membrane wings. AIAA-2010-729, 48th AIAA Aerospace Sciences Meeting, 4-7 January 2010, Orlando, Florida, USA.

Shyy, W., Berg, M., Ljungqvist, D., 1999. Flapping and flexible wings for biological and micro air vehicles. Progress in Aerospace Sciences 35(5), 455-505.

Smith, R., Shyy, W., 1995. Computational model of flexible membrane wings in steady laminar flow. AIAA Journal 33(10), 1769-1777.

Smith, R., Shyy, W., 1996. Computation of aerodynamic coefficients for a flexible membrane airfoil in turbulent flow: a comparison with classical theory. Physics of Fluids 8(12), 3346-3353.

Song, A., Tian, X., Israeli, E., Galvao, R., Bishop, K., Swartz, S., Breuer, K., 2008. Aeromechanics of membrane wings with implications for animal flight. AIAA Journal 46(8), 2096-2106.

Stanford, B., Ifju, P., Albertani, R., Shyy, W., 2008. Fixed membrane wings for micro air vehicles: experimental characterization, numerical modelling, and tailoring. Progress in Aerospace Sciences 44(4), 258-294.

Stanford, B., Sytsma, M., Albertani, R., Viieru, D., Shyy, W., Ifju, P., 2007. Static aeroelastic model validation of membrane micro air vehicle wings. AIAA Journal 45(12), 2828-2837.

Taira, K., Colonius, T., 2009. Three-dimensional flows around low-aspect-ratio flat-plate wings at low Reynolds numbers. Journal of Fluid Mechanics 623, 187-207.

Vickery, B.J., 1968. Load fluctuations in turbulent flow. ASCE Journal of the Engineering Mechanics Division 94, 31.

Wootton, L.R., 1986. The oscillations of model circular stacks due to vortex shedding at Reynolds numbers 10^5 to $3x10^6$. NPL Aero Rep. 1267, National Physical Laboratory, Teddington, U.K.

Wu, J.Z., Lu, X.Y., Denny, A.G., Fan, M., Wu, J.M., 1998. Post-stall flow control on an airfoil by local unsteady forcing. Journal of Fluid Mechanics 371, 21-58.

Table 1
Comparison of previous and present work on frequency of vortex shedding from rigid airfoils and wings.

Wing	t_{max}/c	**Re Number**	**Measurement Station**	**Reference**
AR = 1 and 2, Flat plate	0.0145	Re = 24 300 Re = 36 500 Re = 48 700	$x = 1c$ and $2c$	Present study
AR = 4, NACA0012	0.12	Re = 10 000	$x = 2c$	Calderon et. al, 2010
AR = 10, NACA0012 AR = 10, NACA0012 AR = 10, NACA0012	0.12	Re = 11 126 Re = 20 265 Re = 40 132	$x = 2c$	Huang and Lin, 1995
2-D Thin cambered 2-D Thin cambered 2-D Thin cambered	0.0067	Re = 53 100 Re = 79 700 Re = 106 000	$x = 1c$ and $2c$	Rojratsirikul et al., 2009
2-D Thin flat plate 2-D Thin flat plate	0.03	Re = 15 800 Re = 120 000	$x = 5c$	Fage and Johansen, 1927
2-D Thick flat plate (bevel angle=25°),	0.125	Re = 35 500	not specified $x < c$	Abernathy, 1962
2-D Thick flat plate (bevel angle=30°)	0.2	Re = 11 000 Re = 16 000 Re = 21 000 Re = 32 000	$x = 3.5c$	Chen and Fang, 1996

Figure captions

Figure 1. Power spectra of the membrane oscillations as a function of angle of attack for the two-dimensional airfoil: (a) U_∞ = 5 m/s; (b) U_∞ = 7.5 m/s; (c) U_∞ = 10 m/s. The symbols are the measured shedding frequencies in the wake of an equivalent rigid cambered airfoil.

Figure 2. Schematic of the rectangular wing with cross-section of the rigid frame.

Figure 3. Schematic of deformation measurements using Digital Image Correlation in open-jet wind tunnel.

Figure 4. Schematic of PIV measurements for the streamwise plane at the mid-span.

Figure 5. Magnitude of time-averaged displacement for U_∞ = 5 m/s: (a) $\alpha = 10^o$; (b) $\alpha = 14^o$; (c) $\alpha = 25^o$.

Figure 6. Maximum magnitude of time-averaged displacement as a function of incidence. ▲ U_∞ = 5 m/s; ■ U_∞ = 7.5 m/s; ● U_∞ = 10 m/s.

Figure 7. Magnitude of the time-averaged velocity and streamlines in the mid-span plane for the rectangular wings: (a) rigid wing U_∞ = 5 m/s; (b) membrane wing U_∞ = 5 m/s; (c) membrane wing U_∞ = 10 m/s. Flow is from right to left.

Figure 8. Magnitude of the turbulence intensity in a mid-span plane for the rectangular wings: (a) rigid wing U_∞ = 5 m/s; (b) membrane wing U_∞ = 5 m/s; (c) membrane wing U_∞ = 10 m/s. Flow is from right to left.

Figure 9. Normal force coefficient as a function of incidence for the flexible and rigid rectangular wings. ▲ flexible wing, U_∞ = 5 m/s; ■ flexible wing, U_∞ = 7.5 m/s; ● flexible wing, U_∞ = 10 m/s; △ rigid wing, U_∞ = 5 m/s; □ rigid wing, U_∞ = 7.5 m/s; ○ rigid wing, U_∞ = 10 m/s.

Figure 10. Magnitude of standard deviation of membrane displacement at different incidences: (a) U_∞ = 5 m/s; (b) U_∞ = 7.5 m/s; (c) U_∞ = 10 m/s.

Figure 11. Power spectra of the membrane oscillations as a function of angle of attack for the rectangular wing: (a) U_∞ = 5 m/s; (b) U_∞ = 7.5 m/s; (c) U_∞ = 10 m/s. The symbols correspond to the frequency of vortex shedding from the rigid wing.

Figure 12. Example of spectra of velocity fluctuations in the wake of the wing with aspect ratio AR=2, α = 15°, Re = 48,700.

Figure 13. Strouhal number of vortex shedding for finite wings. + AR=1, flat plate, Re=24 300; × AR=1, flat plate, Re=36 500; ~ AR=1, flat plate, Re=48 700; ☐ AR=2, flat plate, Re=24 300; ○ AR=2, flat plate, Re=36 500; ◇ AR=2, flat plate, Re=48 700; ▲ AR=4, NACA0012, Re=10 000 (Calderon et al., 2010); ● AR=10, NACA0012, Re=11 126 (Huang and Lin, 1995); ■ AR=10, NACA0012, Re=20 265 (Huang and Lin, 1995); ◆ AR=10, NACA0012, Re=40 132 (Huang and Lin, 1995); −−− St = 0.17/sinα.

Figure 14. Strouhal number of vortex shedding for nominally two-dimensional airfoils and wings with sharp leading-edge. + 2-D thin cambered, Re=53 100 (Rojratsirikul et al. 2009); ~ 2-D thin cambered, Re=79 700 (Rojratsirikul et al. 2009); × 2-D thin cambered, Re=106 000 (Rojratsirikul et al. 2009); △ 2-D thin flat plate, Re=15 800 (Fage and Johansen 1927); ☐ 2-D thin flat plate, Re=120 000 (Fage and Johansen 1927); ○ 2-D thick flat plate, Re=11 000 (Chen and Fang 1996); ▽ 2-D thick flat plate, Re=16 000 (Chen and Fang 1996); ◇ 2-D thick flat plate, Re=21 000 (Chen and Fang 1996); ▷ 2-D thick flat plate, Re=32 000 (Chen and Fang 1996); ◆ 2-D thick flat plate, Re=35 500 (Abernathy 1962); −−− St = 0.17/sinα.

Figure 15. Modified Strouhal number of vortex shedding for finite wings. + AR=1, flat plate, Re=24 300; × AR=1, flat plate, Re=36 500; ~ AR=1, flat plate, Re=48 700; □ AR=2, flat plate, Re=24 300; ○ AR=2, flat plate, Re=36 500; ◇ AR=2, flat plate, Re=48 700; ▲ AR=4, NACA0012, Re=10 000 (Calderon et al., 2010); ● AR=10, NACA0012, Re=11 126 (Huang and Lin, 1995); ■ AR=10, NACA0012, Re=20 265 (Huang and Lin, 1995); ◆ AR=10, NACA0012, Re=40 132 (Huang and Lin, 1995).

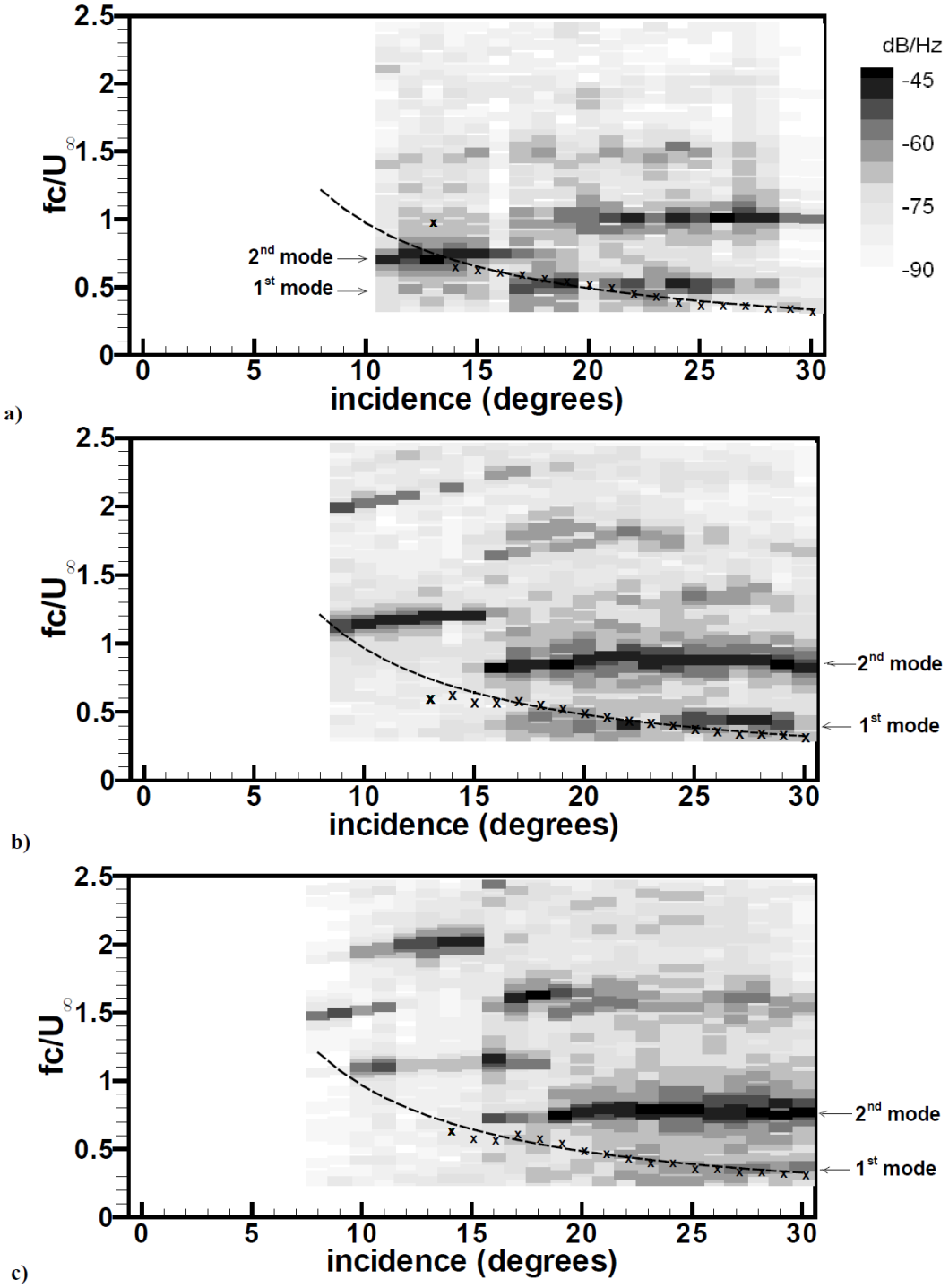

Figure 1. Power spectra of the membrane oscillations as a function of angle of attack for the two-dimensional airfoil: (a) U_∞ = 5 m/s; (b) U_∞ = 7.5 m/s; (c) U_∞ = 10 m/s. The symbols are the measured shedding frequencies in the wake of an equivalent rigid cambered airfoil.

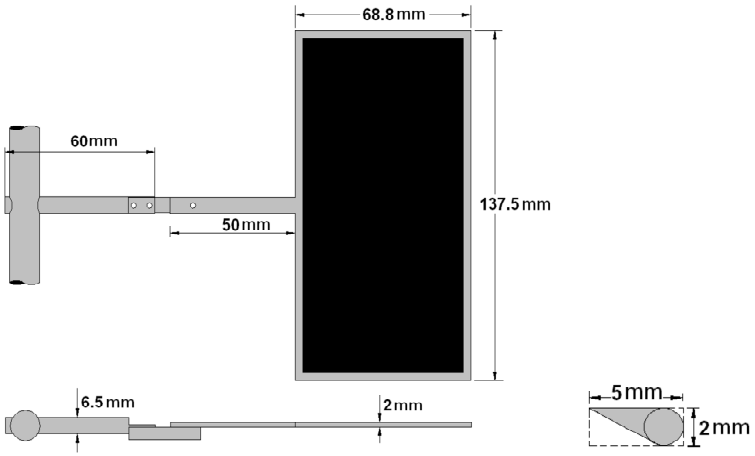

Figure 2. Schematic of the rectangular wing with cross-section of the rigid frame.

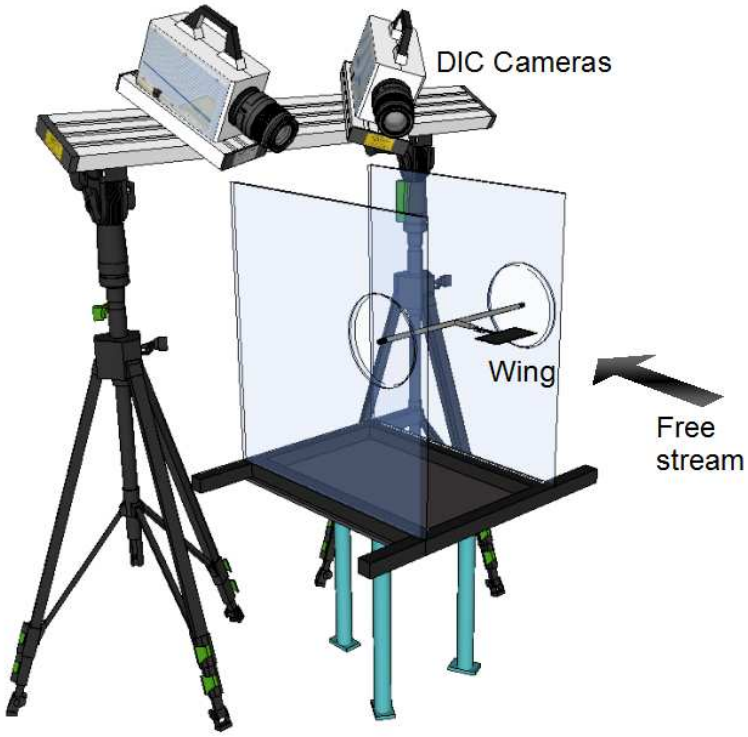

Figure 3. Schematic of deformation measurements using Digital Image Correlation in open-jet wind tunnel.

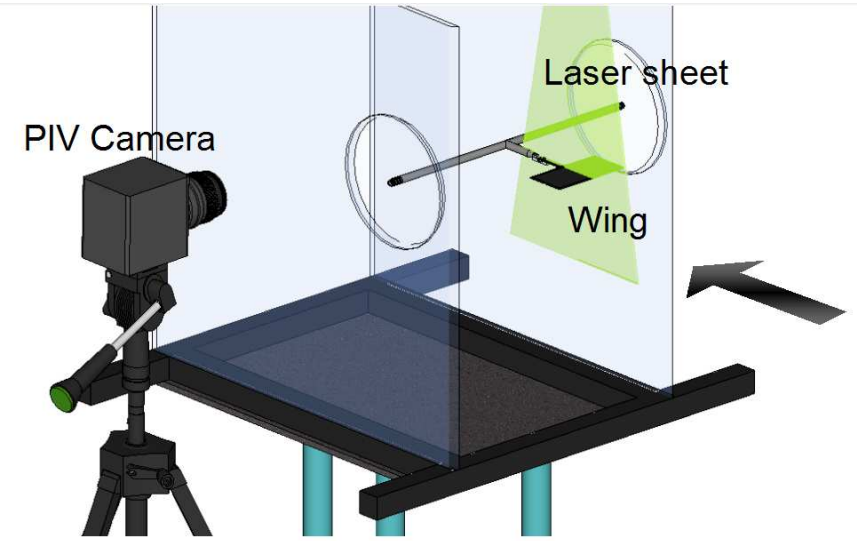

Figure 4. Schematic of PIV measurements for the streamwise plane at the mid-span.

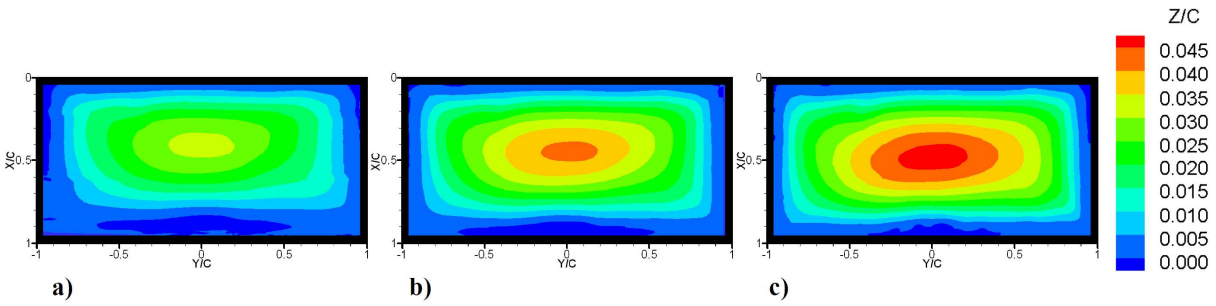

Figure 5. Magnitude of time-averaged displacement for U_∞ = 5 m/s: (a) $\alpha = 10^o$; (b) $\alpha = 14^o$; (c) $\alpha = 25^o$.

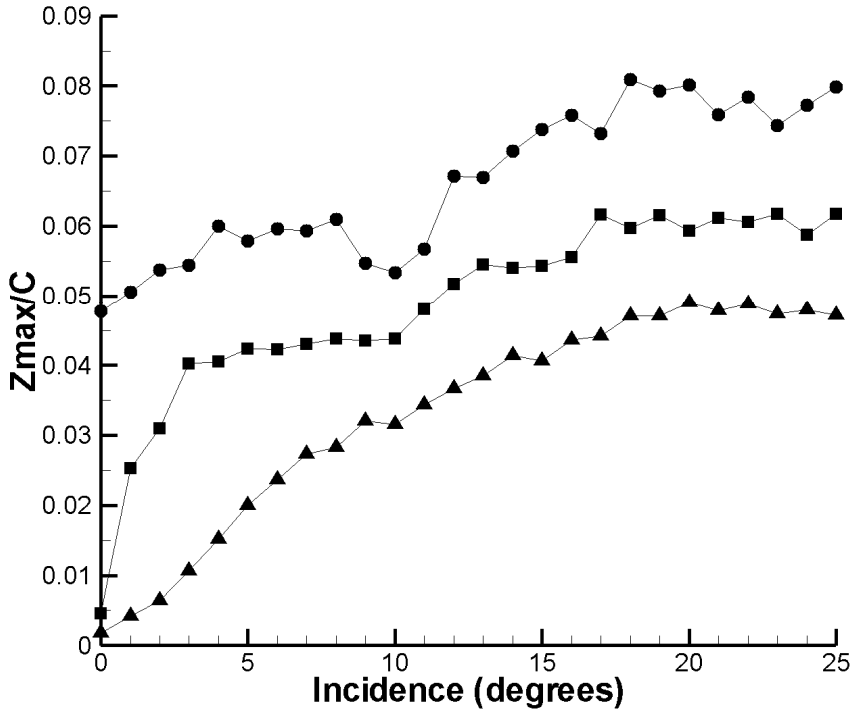

Figure 6. Maximum magnitude of time-averaged displacement as a function of incidence. ▲ U_∞ = 5 m/s; ■ U_∞ = 7.5 m/s; ● U_∞ = 10 m/s.

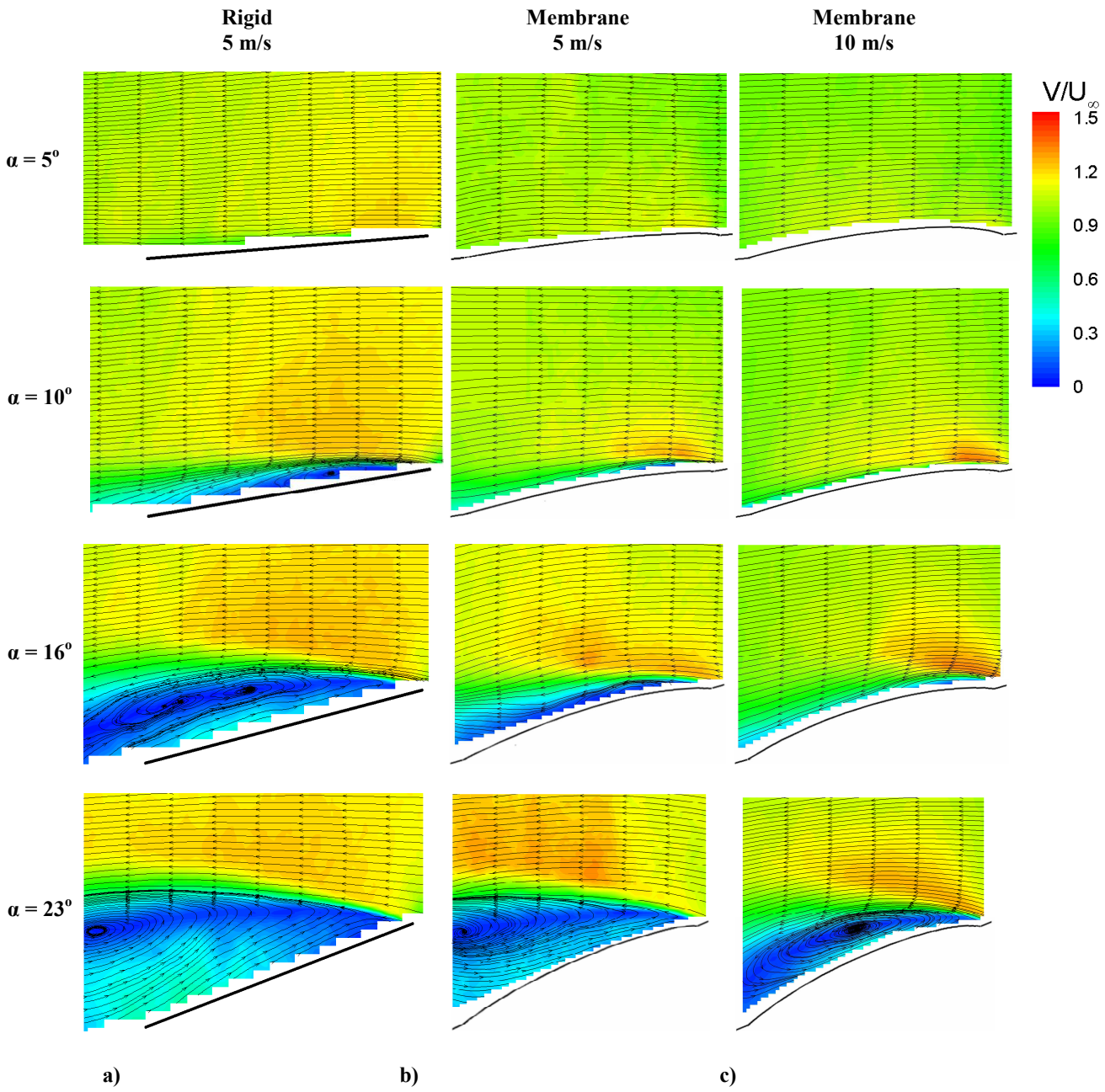

Figure 7. Magnitude of the time-averaged velocity and streamlines in the mid-span plane for the rectangular wings: (a) rigid wing U_∞ = 5 m/s; (b) membrane wing U_∞ = 5 m/s; (c) membrane wing U_∞ = 10 m/s. Flow is from right to left.

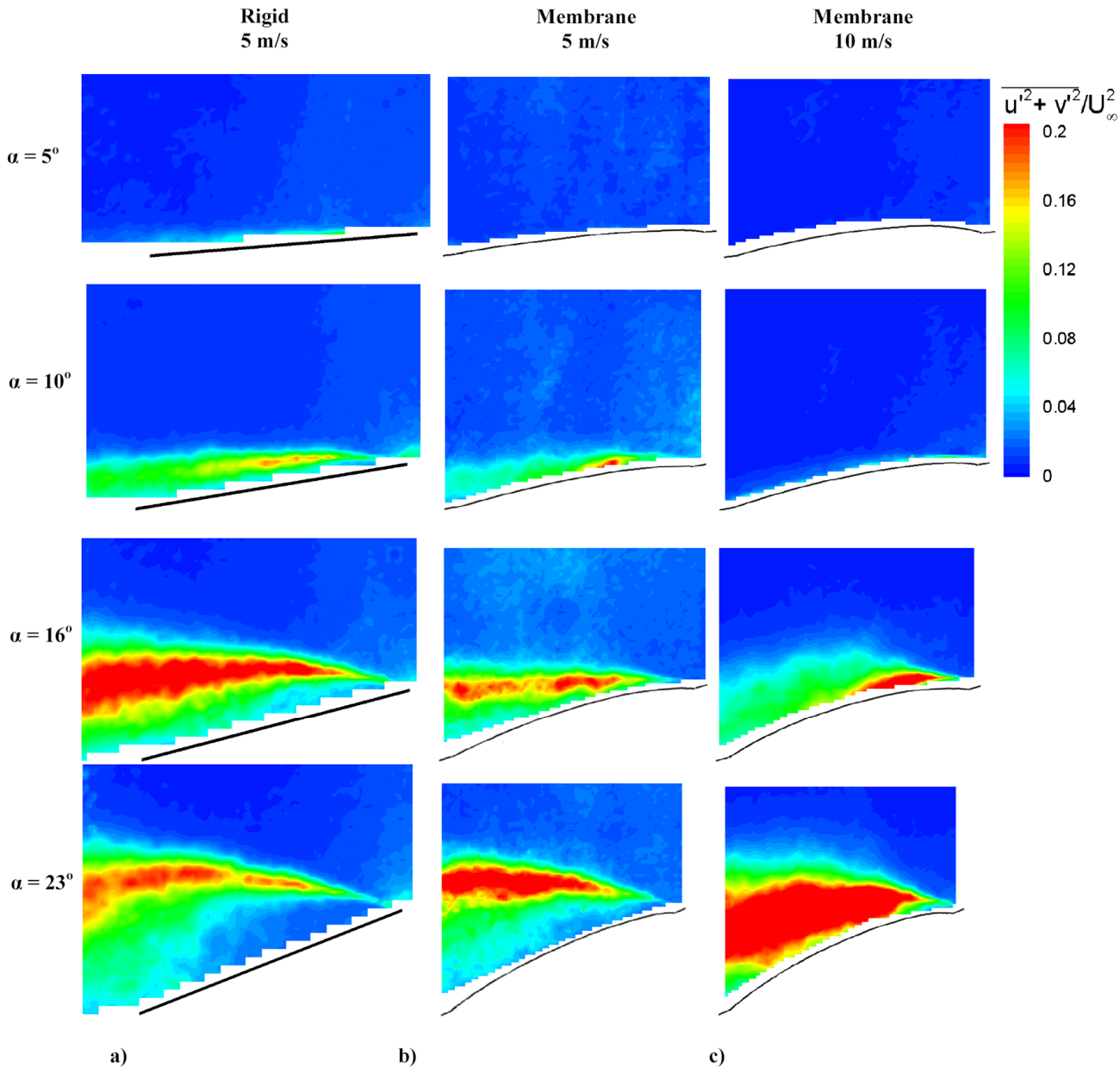

Figure 8. Magnitude of the turbulence intensity in a mid-span plane for the rectangular wings: (a) rigid wing U_∞ = 5 m/s; (b) membrane wing U_∞ = 5 m/s; (c) membrane wing U_∞ = 10 m/s. Flow is from right to left.

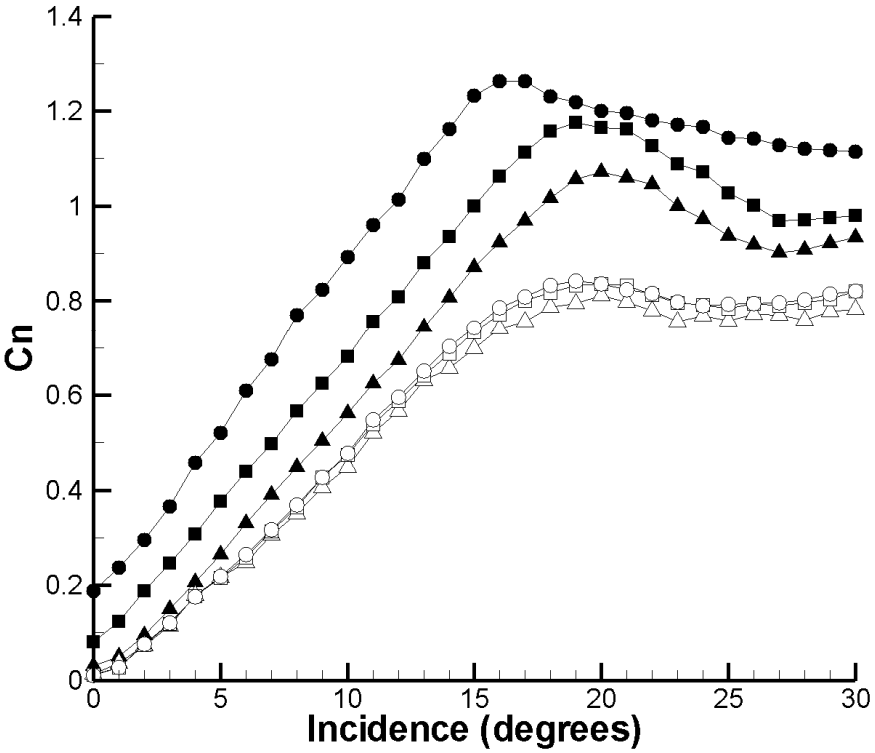

Figure 9. Normal force coefficient as a function of incidence for the flexible and rigid rectangular wings. ▲ flexible wing, U_∞ = 5 m/s; ■ flexible wing, U_∞ = 7.5 m/s; ● flexible wing, U_∞ = 10 m/s; △ rigid wing, U_∞ = 5 m/s; □ rigid wing, U_∞ = 7.5 m/s; ○ rigid wing, U_∞ = 10 m/s.

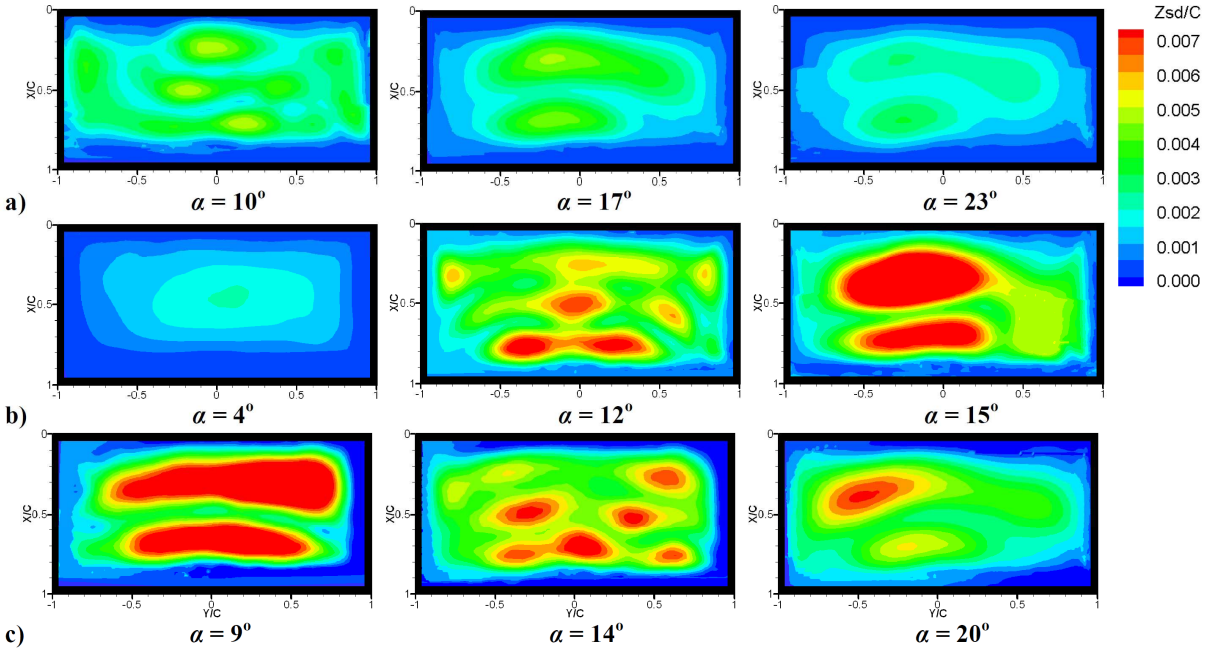

Figure 10. Magnitude of standard deviation of membrane displacement at different incidences: (a) U_∞ = 5 m/s; (b) U_∞ = 7.5 m/s; (c) U_∞ = 10 m/s.

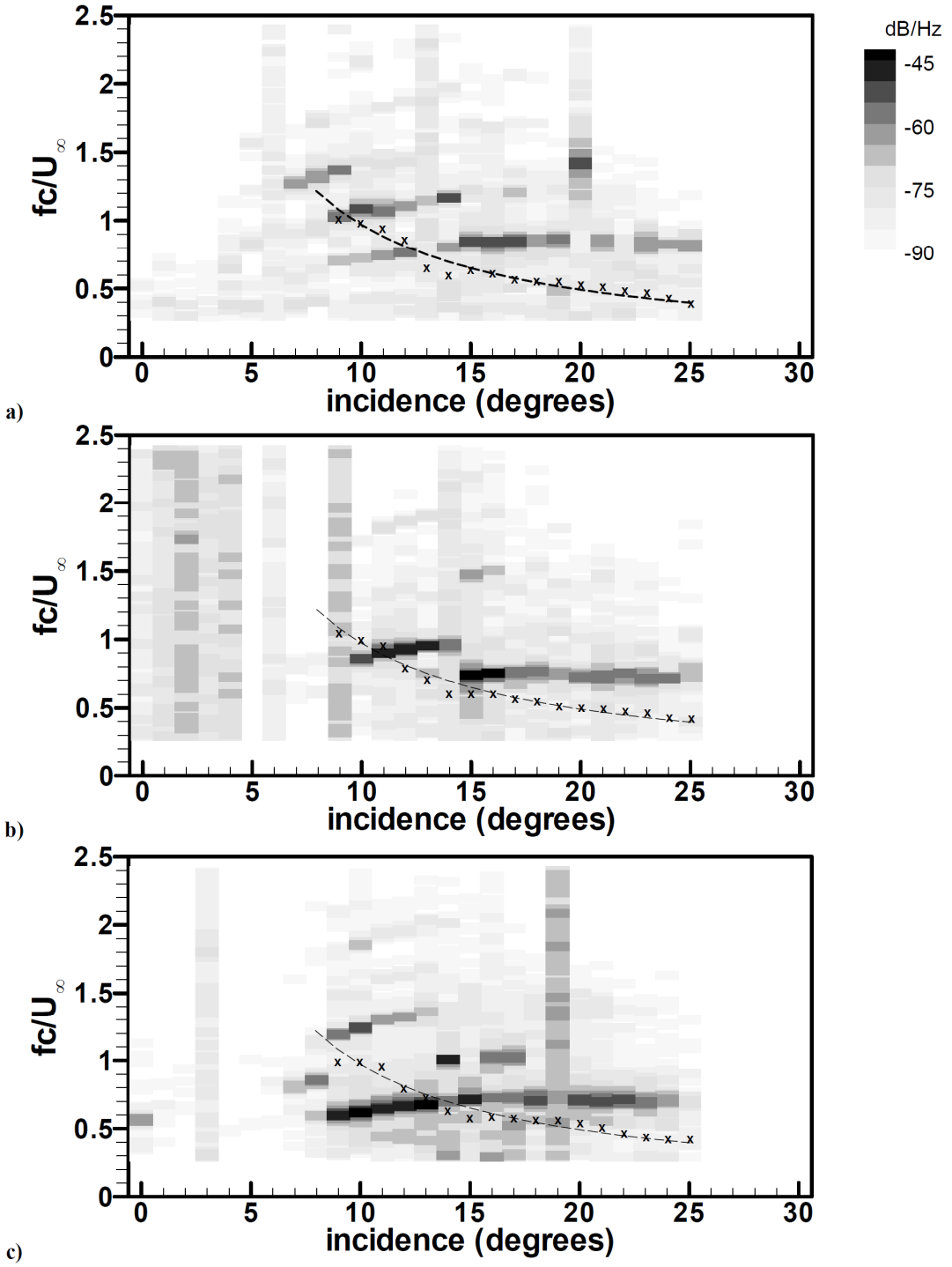

Figure 11. Power spectra of the membrane oscillations as a function of angle of attack for the rectangular wing: (a) U_∞ = 5 m/s; (b) U_∞ = 7.5 m/s; (c) U_∞ = 10 m/s. The symbols correspond to the frequency of vortex shedding from the rigid wing.

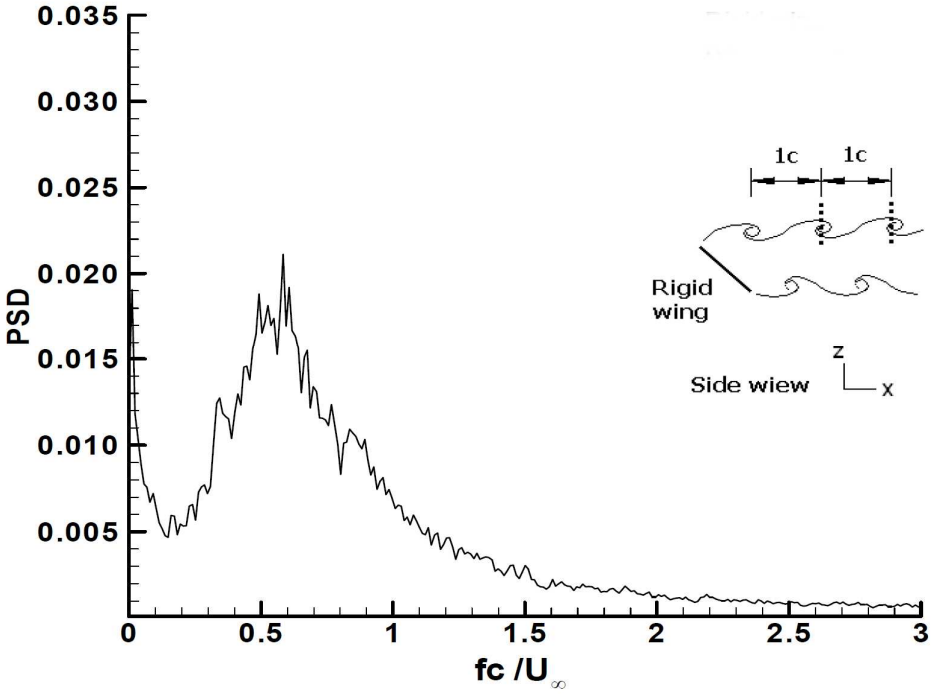

Figure 12. Example of spectra of velocity fluctuations in the wake of the wing with aspect ratio AR=2, α = 15°, Re = 48,700.

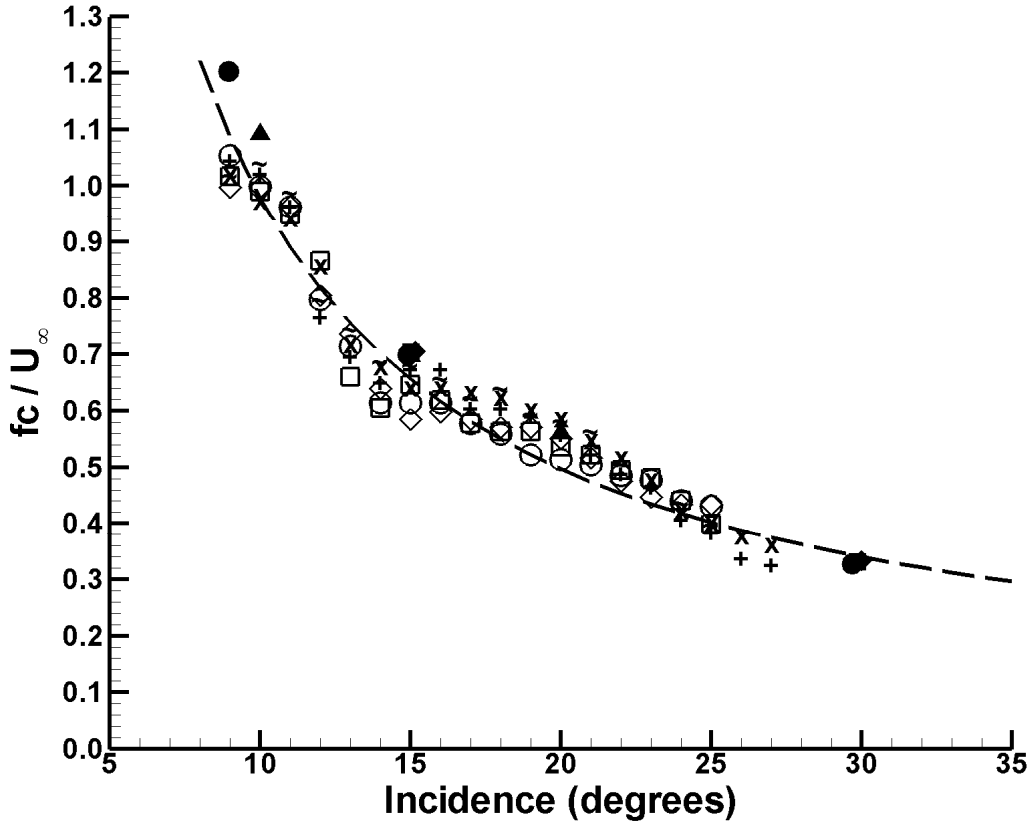

Figure 13. Strouhal number of vortex shedding for finite wings. + AR=1, flat plate, Re=24 300; × AR=1, flat plate, Re=36 500; ~ AR=1, flat plate, Re=48 700; □ AR=2, flat plate, Re=24 300; ○ AR=2, flat plate, Re=36 500; ◇ AR=2, flat plate, Re=48 700; ▲ AR=4, NACA0012, Re=10 000 (Calderon et al., 2010); ● AR=10, NACA0012, Re=11 126 (Huang and Lin, 1995); ■ AR=10, NACA0012, Re=20 265 (Huang and Lin, 1995); ◆ AR=10, NACA0012, Re=40 132 (Huang and Lin, 1995); −−− St = 0.17/sinα.

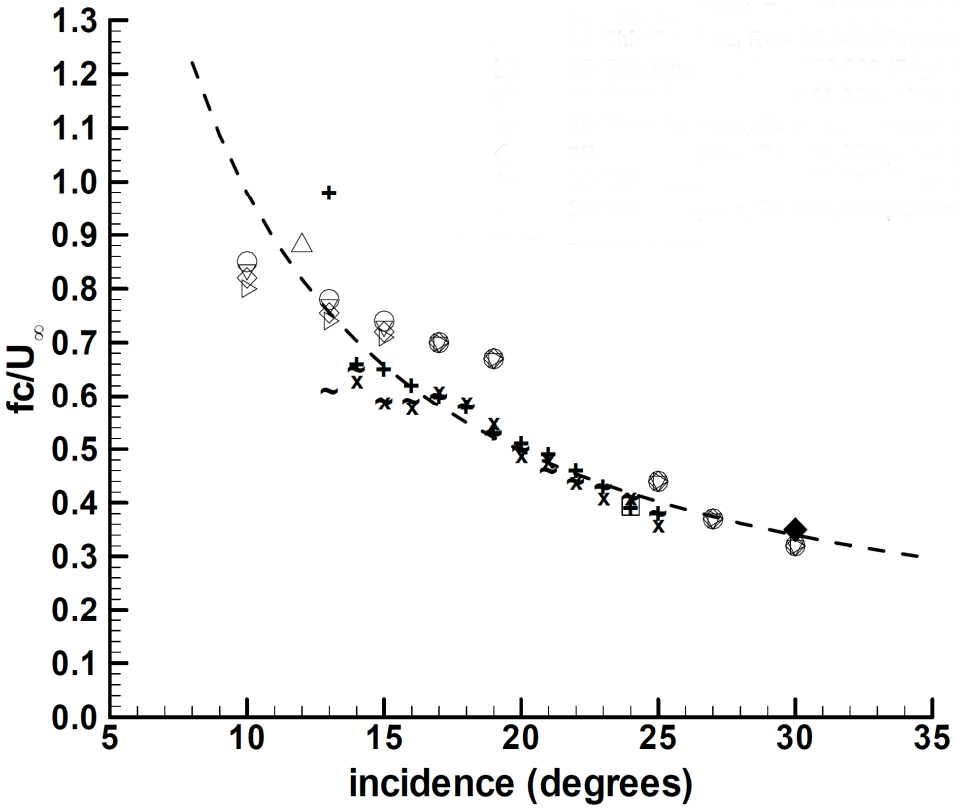

Figure 14. Strouhal number of vortex shedding for nominally two-dimensional airfoils and wings with sharp leading-edge. + 2-D thin cambered, Re=53 100 (Rojratsirikul et al. 2009); ~ 2-D thin cambered, Re=79 700 (Rojratsirikul et al. 2009); × 2-D thin cambered, Re=106 000 (Rojratsirikul et al. 2009); △ 2-D thin flat plate, Re=15 800 (Fage and Johansen 1927); □ 2-D thin flat plate, Re=120 000 (Fage and Johansen 1927); ○ 2-D thick flat plate, Re=11 000 (Chen and Fang 1996); ▽ 2-D thick flat plate, Re=16 000 (Chen and Fang 1996); ◇ 2-D thick flat plate, Re=21 000 (Chen and Fang 1996); ▷ 2-D thick flat plate, Re=32 000 (Chen and Fang 1996); ◆ 2-D thick flat plate, Re=35 500 (Abernathy 1962); −−− St = 0.17/sinα.

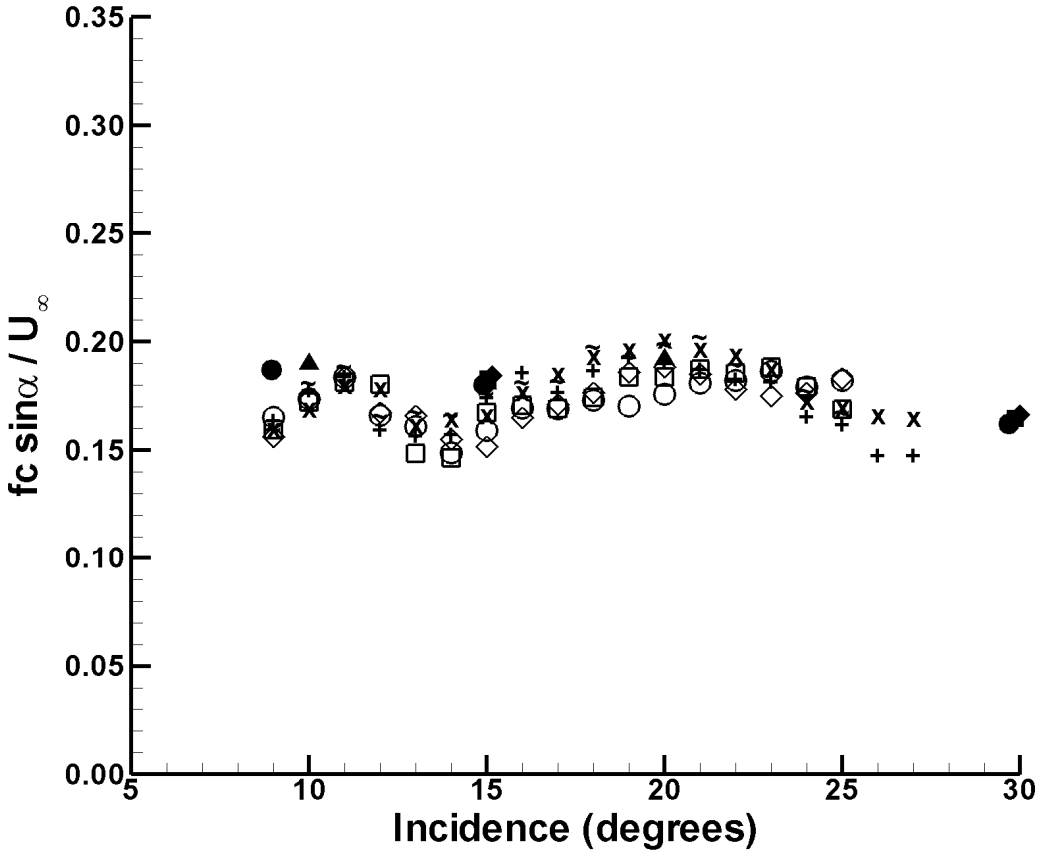

Figure 15. Modified Strouhal number of vortex shedding for finite wings. + AR=1, flat plate, Re=24 300; × AR=1, flat plate, Re=36 500; ~ AR=1, flat plate, Re=48 700; □ AR=2, flat plate, Re=24 300; ○ AR=2, flat plate, Re=36 500; ◇ AR=2, flat plate, Re=48 700; ▲ AR=4, NACA0012, Re=10 000 (Calderon et al., 2010); ● AR=10, NACA0012, Re=11 126 (Huang and Lin, 1995); ■ AR=10, NACA0012, Re=20 265 (Huang and Lin, 1995); ◆ AR=10, NACA0012, Re=40 132 (Huang and Lin, 1995).